AGU ADVANCING EARTH AND SPACE SCIENCES

Geophysical Research Letters

RESEARCH LETTER
10.1029/2025GL117377

Key Points:

- We identify long, weak seismic radiation with enhanced high-frequency signals for the M_W 7.5 and M5+ earthquakes in the Noto region
- Heterogeneous rupture with isolated asperities in the weak fluid-bearing fault zone is responsible for the abnormal seismic radiation
- The multi-asperity rupture model holds implications for seismic radiation of subduction zone large earthquakes and low-frequency earthquakes

Supporting Information:

Supporting Information may be found in the online version of this article.

Correspondence to:

L. Ye,
yell@sustech.edu.cn

Citation:

Yao, S., Ye, L., Yang, H., & Xia, T. (2025). Diverse rupture behaviors of M5 earthquakes reveal heterogeneous fluid effects in Noto Peninsula, central Japan. *Geophysical Research Letters*, *52*, e2025GL117377. https://doi.org/10.1029/2025GL117377

Received 2 JUN 2025
Accepted 13 OCT 2025

Author Contributions:

Conceptualization: Lingling Ye
Formal analysis: Suli Yao, Lingling Ye
Funding acquisition: Lingling Ye, Hongfeng Yang
Investigation: Suli Yao
Methodology: Tao Xia
Validation: Suli Yao
Visualization: Suli Yao
Writing – original draft: Suli Yao, Lingling Ye
Writing – review & editing: Suli Yao, Lingling Ye, Hongfeng Yang

Diverse Rupture Behaviors of M5 Earthquakes Reveal Heterogeneous Fluid Effects in Noto Peninsula, Central Japan

Suli Yao[1,2], Lingling Ye[1], Hongfeng Yang[2,3], and Tao Xia[1]

[1]Department of Earth and Space Sciences, Southern University of Science and Technology, Shenzhen, China, [2]Department of Earth and Environmental Sciences, The Chinese University of Hong Kong, Hong Kong, China, [3]Shenzhen Research Institute, The Chinese University of Hong Kong, Shenzhen, China

Abstract The 15-s-long weak initial rupture of the 2024 M_W 7.5 Noto earthquake overlapped with a fluid-rich region of a preceding earthquake swarm and was accompanied by enhanced high-frequency seismic radiation. To understand the radiation and related source processes, we investigate rupture behaviors of four nearby M5+ events. We find that the 5 May 2023 M_W 5.7 event exhibits similar characteristic radiation, resulting in a relatively low source spectral decay rate. Apparent moment-rate functions and dynamic rupture simulations, constrained from near-source waveform data, consistently suggest a northeastward rupture with multiple asperities. Such rupture heterogeneities under a fluid-rich condition can explain the weak, long seismic radiation but with enhanced high-frequency signals in the M_W 5.7 event and the initial rupture of the 2024 M_W 7.5 Noto earthquake. The multi-asperity model also holds implications for other observations, including the depth dependence of high-frequency radiation and the low spectral falloff rates observed for low-frequency earthquakes.

Plain Language Summary On 1 January 2024, an M_W 7.5 event initiated beneath the Noto Peninsula in central Japan. A striking feature of this event is its strong high-frequency radiation during its 15-s-long weak initial rupture that spanned a fluid-rich region with an earthquake swarm persisting since 2022. To understand this weak, long seismic radiation with enhanced high-frequency content, we investigate 4 nearby M5+ earthquakes. We rule out the path effects with the empirical green function using nearby small earthquakes and confirm the enhanced high-frequency source radiation during the 5 May 2023 M_W 5.7 earthquake. Based on apparent moment-rate functions in the time domain and dynamic modeling, we propose a rupture model with multiple asperities for this M_W 5.7 event. We deduce that ruptures of small isolated asperities could be responsible for the enhanced high-frequency radiation in the initial rupture of the 2024 M_W 7.5 event. Our study highlights rupture heterogeneities and the associated seismic observations under a fluid-rich condition.

1. Introduction

Since November 2022, an intense swarm has persisted within a reverse fault system beneath the northeastern Noto Peninsula, Japan. Multiple studies of the seismicity (Amezawa et al., 2023; Fukuoka et al., 2024; Hirose et al., 2024; Kato, 2024; Kumazawa & Ogata, 2024; Matsumoto & Yoshida, 2024; Ogata & Kumazawa, 2024; Peng et al., 2025; Takano et al., 2024; Yoshida et al., 2024), the velocity structure (Nakajima, 2022; Okada et al., 2024; Wang et al., 2024; Yoshida, Uno, et al., 2023), the geodetic deformation field (Nishimura et al., 2023), and the geochemical signatures (Umeda et al., 2024) suggest that the swarm region has been experiencing fluid diffusion originating from downdip and possible aseismic slip. On 1 January 2024, an M_W 7.5 event initiated from the swarm region and propagated bilaterally with a final extent of ∼150 km (Fujii & Satake, 2024; Fukushima et al., 2024; Guo et al., 2024; Kutschera et al., 2024; Ma et al., 2024; Okuwaki et al., 2024; Shinohara et al., 2025; Xu et al., 2024; Yang et al., 2024), resulting in violent ground shaking and a tsunami (Suppasri et al., 2024; Yamanaka et al., 2024). A striking feature of this event is its 15-s-long weak and slow initial expanding (i.e., 0.5–1.0 km/s) within the swarm region (Aochi, 2024; Liu et al., 2024; Ma et al., 2024; Okuwaki et al., 2024; Xu et al., 2024; Yamada et al., 2025). Particularly, this weak and slow rupture stage is accompanied by rich high-frequency seismic signals as revealed by teleseismic back-projection (BP) analyses (Ma et al., 2024; Xu et al., 2024) and local strong-motion data (Figure 1c). The mechanism for this weak and slow seismic radiation with enhanced high-frequency content in the fluid-rich condition is intriguing.

10.1029/2025GL117377

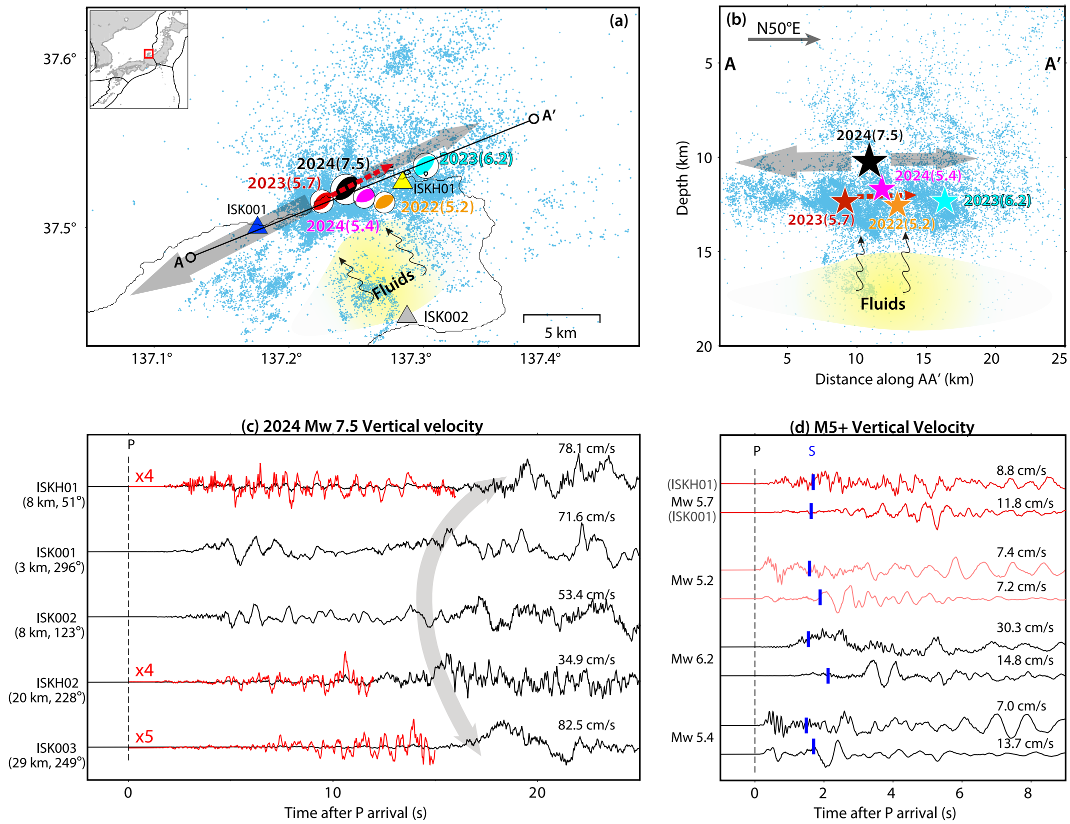

Figure 1. *The distribution of M*5.0+ *events in the Noto region from 2022 to 2024 and nearby strong-motion observations.* (a) Focal mechanisms of M5.0+ events from the NIED catalog with locations from Yoshida et al. (2024) and seismicity (blue dots) from March 2003 to the 2024 M_W 7.5 mainshock (Yoshida et al., 2024). The triangles show the locations of local strong-motion stations. The gray arrows indicate the rupture propagation of the 2024 M_W 7.5 event. The inset panel is the regional map with major plate boundaries (black lines). (b) A vertical cross-sectional view along the direction of N50°E (AA'). The stars denote the hypocenters of M5.0+ events. (c) Vertical velocity waveforms for the 2024 M_W 7.5 event at local strong-motion stations (station locations in Figure S1). (d) Vertical velocity waveforms for the four M5.0+ events at stations ISK001 and ISKH01. The waveforms are aligned by the manually picked P arrivals, with peak velocity amplitudes marked to the right.

Understanding high-frequency seismic signals is essential as it largely controls ground shaking intensity. However, given complexities of large earthquakes, elucidating the exact origins of high-frequency content remains challenging. Therefore, instead of the 2024 M_W 7.5 mainshock, here we focus on four nearby M5+ earthquakes (Figures 1a and 1b), including the 19 June 2022 M_W 5.2 event, the 05 May 2023 M_W 6.2 event, the 05 May 2023 M_W 5.7 event, and the 01 January 2024 M_W 5.4 foreshock that occurred 10 min prior to the mainshock. At two local strong-motion stations (ISKH01 and ISK001), we observe similar weak, prolonged high-frequency waves for the 2023 M_W 5.7 event (Figure 1d). In this study, we investigate the source characteristics of the four M5+ events, with a particular focus on the 2023 M_W 5.7 event.

2. Spectral Characteristics of M5+ Earthquakes

We conduct spectral analyses for the four M5+ events utilizing data from KiK-net and K-NET strong-motion networks operated by the National Research Institute for Earth Science and Disaster Prevention, Japan (NIED) (Figure 2a). To obtain the source spectra, we apply nearby smaller earthquakes as empirical Green's functions (EGFs) to represent propagation and site effects. We consider EGF events featuring similar reverse faulting mechanisms with target events. Recordings at stations located 20–150 km from the sources are considered. Ultimately, we identify 2 EGF events for the 2022 M_W 5.2 event, 3 EGF events for the 2023 M_W 6.2 event, 4 EGF events for the 2023 M_W 5.7 event, and 2 EGF events for the 2024 M_W 5.4 event (Figures S1–S11 in Supporting

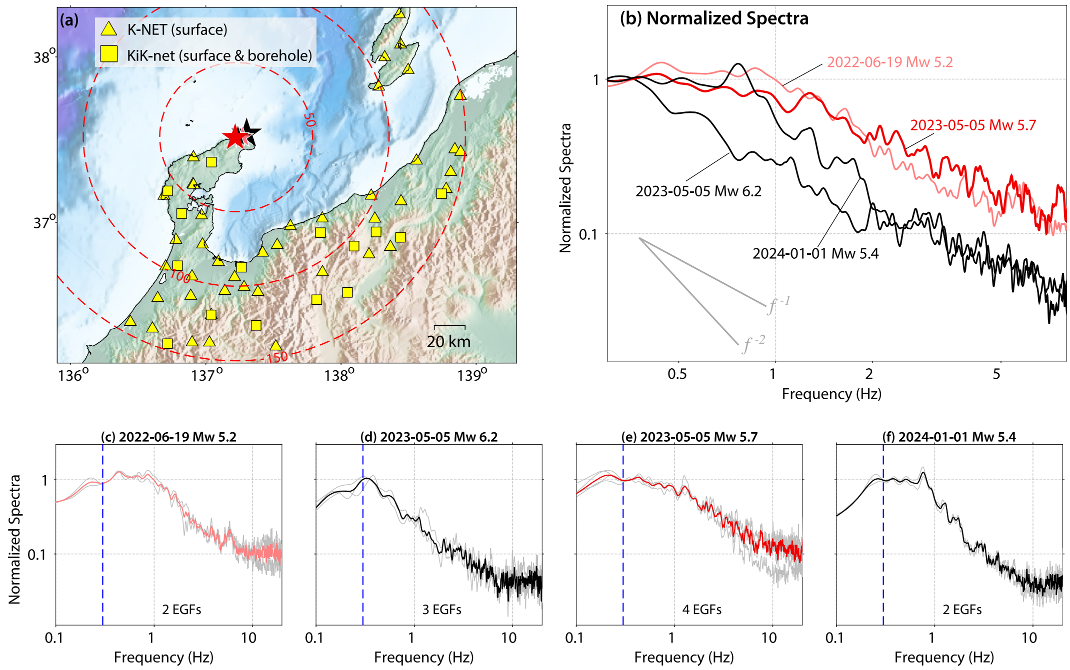

Figure 2. *Spectra analysis for the four M5.0+ events using S waves*. (a) The distribution of four M5.0+ earthquakes (stars) and regional strong motion stations within 150 km (yellow triangles and squares). The hypocenters of the 2023 M_W 5.7 and the 2022 M_W 5.2 events are marked in red and light red, respectively. The hypocenters of the other two events are marked in black. (b) The average empirical Green's function (EGF)-corrected source spectra of the four M5.0+ earthquakes, with spectral amplitudes normalized against the corresponding average level in the frequency band of 0.3–0.4 Hz. (c–f) The source spectra corrected using different EGFs (gray) and their average spectra for the four M5.0+ events, respectively. The spectra of the M_W 5.7 event and the M_W 5.2 events are plotted in red and light red respectively to emphasize the potential abnormal falloff rates. The dashed blue lines mark the potential truncation frequency of 0.3 Hz.

Information S1). Consistent spectral ratios with different EGF events suggest that the first-order feature in the spectral shape is robust (Figure 2).

For each target event and each EGF event, we calculate the spectral ratios using *P*- and *S*-wave windows. We select data with signal-to-noise ratios (SNRs) higher than 3 in the frequency band of 0.3–10 Hz. The P window starts 2 s before the P arrival and ends 1 s before the S arrival, and a minimum window length of 5 s is required to ensure that the entire P phase is captured. However, after applying this criterion, the qualified *P*-wave traces of EGF events are inadequate for a robust analysis. Consequently, we use *S* waves for the EGF corrections. The *S*-wave window starts 2 s before the S arrival with a length of 20 s. We then normalize the *S*-wave spectra according to their average amplitudes in the frequency band of 0.3–0.4 Hz. Finally, we take the average spectra corrected by different EGF events as the source spectra (Figures 2b–2f). Detailed spectral ratio calculation results are presented in Figures S1–S11 in Supporting Information S1.

Earthquake source spectra can be represented by a generalized Brune's model (Brune, 1970):

$$S(f) = \frac{M_0}{1 + \left(f/f_c\right)^n} \tag{1}$$

where the spectrum (S) is characterized by the seismic moment (M_0), the corner frequency (f_c) related to the source duration, and the logarithmic falloff rate (n). As shown in Figure 2b, it appears that all spectra fall off linearly to 8 Hz, above which the spectra start turning flat (Figures 2c–2f). This cutoff frequency corresponds to the corner frequencies of the EGF events. Below 8 Hz, the source spectra are nearly free of bias from EGF events.

We roughly determine the corner frequencies (f_c) of the 2022 M_W 5.2 event and the 2024 M_W 5.4 event by fitting the spectra using Equation 1 in the frequency bin of 0.3–5 Hz, which covers the low-frequency plateau and avoids the high-frequency contributions of EGFs. The optimal f_c are 1.5 Hz and 1.0 Hz with falloff rates of 2.0 and 1.9 for

10.1029/2025GL117377

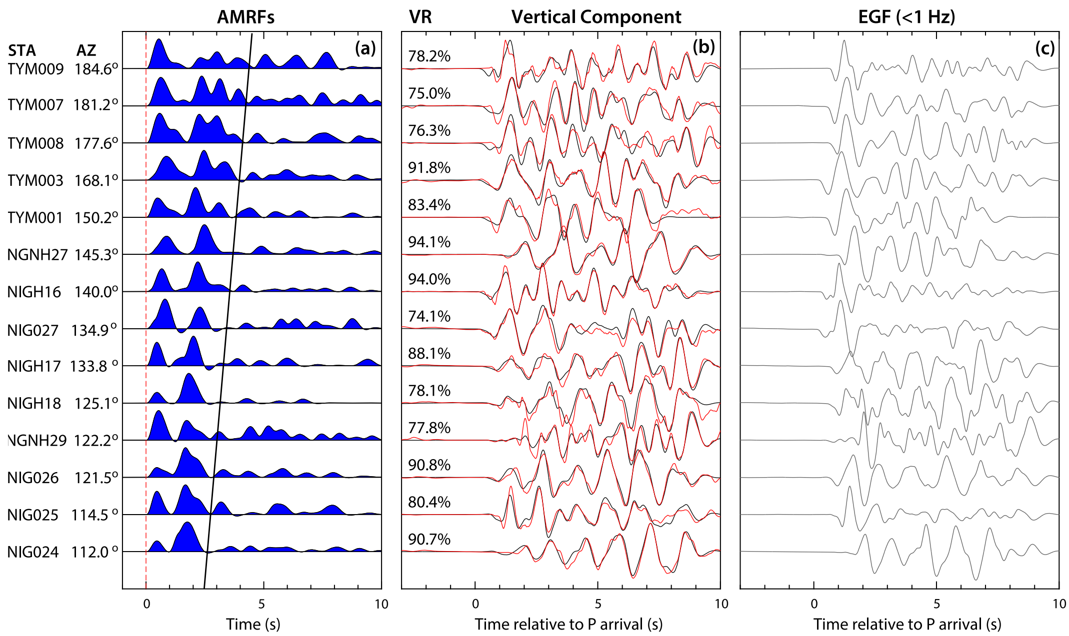

Figure 3. *Apparent moment rate function (AMRF) deconvolution results for the 2023 M_W 5.7 event*. (a) AMRFs of the M_W 5.7 mainshock using the empirical Green's function (EGF) event on 8 March 2022 (M_W 4.7; EGF1), with station names (STA) and azimuths (AZ) labeled. The black solid line indicates the possible rupture directivity effect. (b) The synthetic (red) and observed (black) vertical *P* waves lowpass filtered with 1 Hz for the mainshock, respectively. (c) The vertical *P* waves of the EGF event, lowpass filtered with 1 Hz.

the M_W 5.2 and the M_W 5.4 events, respectively. Due to the poor instrumental response below 0.3 Hz, we do not obtain a clear low-frequency spectral plateau for the M_W 5.7 and M_W 6.2 events, indicating potential f_c close to or below 0.3 Hz. Previous studies using seismic and geodetic data suggest a total duration of ∼10 s with a 6-s-long major energy pulse for the M_W 6.2 event (Asano & Iwata, 2025; Liu et al., 2024; Yoshida, Uchida, et al., 2023), while the source process of the M_W 5.7 event remains unexplored.

Particularly, the source spectra of the M5+ events exhibit varying falloff rates (Figure 2b). The source spectrum of the 2023 M_W 5.7 event decays obviously slower compared to the 2023 M_W 6.2 and the 2024 M_W 5.4 events, while the 2022 M_W 5.2 event falls between them (Figure 2b). Notably, the local strong-motion records for the M_W 5.2 event also exhibit prolonged waves, though less pronounced than those in the M_W 5.7 event (Figure 1d). To further validate the results of different falloff rates and its dependence on seismic phases (P and S), we calculate the spectral ratios between those M5+ events (Figures S12–S15 in Supporting Information S1) with the 2023 M_W 5.7 event as the numerator using the *P*-wave window, *S*-wave window, and the window that includes both P and S phases (a 35-s-long window starting 2 s before the P arrival). As shown in Figure S15 in Supporting Information S1, the spectral ratios commonly feature a slope of f^1 in the frequency band of 0.5–2 Hz no matter which time window is used. The spectral decay rates above 2 Hz in those 4 M5+ events are similar, as indicated by their nearly flat spectral ratios (Figure S15 in Supporting Information S1). The relative intensity of the high-frequency content above 2 Hz scales with the moment magnitude: the M_W 5.7 event exhibits stronger radiation than the M_W 5.2 and M_W 5.4 events, but weaker than the M_W 6.2 event.

3. Apparent Moment Rate Functions of the 2023 M_W 5.7 Event

To investigate the rupture process of the 2023 M_W 5.7 event, we adopt the EGF method to calculate the apparent moment-rate functions (AMRFs) through time-domain deconvolutions, following a similar procedure proposed by Ye et al. (2020) and Gong et al. (2022). The 8 March 2022 M_W 4.7 event is selected as the EGF event (EGF1) (Figure S16 in Supporting Information S1). We use vertical P acceleration waveforms windowed starting 5 s before the P arrivals and ending before the S arrivals for deconvolutions (Figures 3b and 3c). Waveforms are filtered to below 1 Hz. With a positivity constraint, we obtain 14 AMRFs in the azimuthal range from 112° to 185° with variance reductions exceeding 75% in waveform fitting (Figure 3).

The AMRFs feature 2 primary energy pulses with total durations of 2.5–4.5 s (Figure 3a). Stations located in the south tend to have more energy pulses and longer durations (Figure 3a). To examine the robustness, we perform deconvolutions using 3 other EGF events, including the 3 October 2021 M_W 3.9 (EGF2), 21 December 2021 M_W 3.9 (EGF3), and 4 April 2022 M_W 4.1 (EGF4). Although the numbers of AMRFs are limited, the results align well with the results using EGF1 regarding major energy pulses and durations (Figure S16 in Supporting Information S1). In addition, we test deconvolutions with lowpass filters of 0.5 Hz and 2 Hz. The results of 0.5 Hz exhibit 2 stable energy pulses (Figure S17 in Supporting Information S1), and the results of 2 Hz demonstrate instability characterized by multiple 0.5-s-long energy spikes (Figure S18 in Supporting Information S1), while the azimuthal dependence of the total duration remains. Overall, the AMRFs suggest a complex energy release process (Figure 3a).

We then conduct directivity analysis based on the AMRFs. We calculate the directivity parameters for each station, $\zeta = p\cos(\theta_{\mathrm{sta}} - \theta_{\mathrm{rup}})$, in which p is the ray parameter, θ_{sta} is the station azimuth, and θ_{rup} is the azimuth of the average rupture direction. The durations of AMRFs (T) should be proportional to ζ, $T = T_0 + \zeta L$, in which T_0 is the true rupture duration and L is the rupture length. Using the durations of AMRFs as the constraint, we search for the optimal L and θ_{rup}. The minimum residual is achieved with θ_{rup} of N60°E and L of 8 km (Figure S19 in Supporting Information S1). Due to the limited azimuthal coverage of AMRFs, θ_{rup} in the range of N20°E–N100°E can fit the durations nearly equally with a rupture length of 8–12 km (Figure S19 in Supporting Information S1).

4. Dynamic Rupture Models With Near-Source Observations

We further investigate the source process of the M_W 5.7 event using near-source observations and dynamic rupture models. The two nearest strong-motion stations, ISK001 and ISKH01, are located within 10 km from the epicenter. We find atypical multiple wiggles and prolonged durations in recordings of the M_W 5.7 event (Figure 1d). Such feature is absent in the recordings for other M5+ events (Figure 1d), ruling out strong site effects. Here, we conduct dynamic rupture simulations for the M_W 5.7 event and constrain the models using data at stations ISK001 and ISKH01.

A 3-D elastic domain with an embedded reverse planar fault is constructed. The model domain extends 40 km along the strike, 40 km along the strike-normal direction, and 30 km in the vertical direction. The embedded fault extends 15 km along the strike and 20 km in the strike-normal direction with the strike (i.e., N50°E) and the dip angle (i.e., 40°) following the focal mechanism of the M_W 5.7 event reported by NIED. The grid size is 50 m on the fault and gradually increases to 1 km at domain boundaries. A layered velocity model that combines the local shallow-5-km velocity structure (https://www.j-shis.bosai.go.jp/map/JSHIS2/download.html?lang=en) and the CRUST1.0 model (Laske et al., 2013) is adopted to prescribe material properties (Table S1 in Supporting Information S1).

A linear slip-weakening law is adopted as the constitutive law on the fault, in which the frictional strength (τ_f) decreases linearly with the slip (ξ) from the static friction (τ_s) to the dynamic friction (τ_d) within the critical weakening distance (D_c):

$$\tau_f(\xi) = \begin{cases} \tau_s - \dfrac{\xi}{D_c} \times (\tau_s - \tau_d), & \xi < D_c \\ \tau_d, & \xi \geq D_c \end{cases} \quad (2)$$

We set D_c and τ_d to be 0.1 m and 20 MPa, respectively. We prescribe the initial shear stress (τ_i) to be purely reverse with a background level of 20 MPa and extra stress inside asperities. The effective normal stress (σ_n) is prescribed to be 100 MPa. The yield stress τ_s is set according to the initial shear stress (τ_i) distribution, controlled by a stress ratio (S):

$$(\tau_s - \tau_i) = S * (\tau_i - \tau_d) \quad (3)$$

We assume S to be 1. To confine the rupture extent, we set a high τ_s of 200 MPa outside asperities. Ruptures are nucleated at the hypocentral depth of 12.3 km with an initial rupture speed of 3 km/s. A time step of 0.002 s is

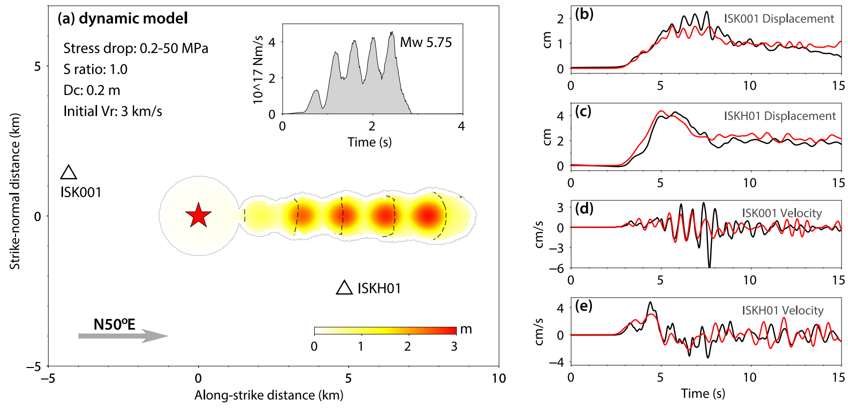

Figure 4. *A multi-asperity dynamic rupture model for the 2023 M_W 5.7 earthquake*. (a) The final slip, nucleation site (red star), rupture contours every 0.5 s, and moment-rate function of the dynamic model. The triangles denote the locations of two near-source stations ISK001 and ISKH01. (b, c) The synthetic (red) and observed (black) vertical displacement at stations ISK001 and ISKH01. (d, e) The synthetic (red) and observed (black) vertical velocity waveforms at stations ISK001 and ISKH01. The time zero is the earthquake origin time. Both the data and synthetic waveforms are low-pass filtered below 2 Hz.

adopted. We use the open-source finite-element tool PyLith (Aagaard et al., 2013) to run the fully dynamic rupture simulations.

We first test two-asperity models (Figure S20 in Supporting Information S1) with rupture directions of N10°E, N50°E, and N90°E and rupture lengths of ∼10 km, as informed by the AMRFs. The moment magnitudes are 5.76 with total source durations of ∼3.4 s, comparable to the estimates from AMRFs. The average rupture speed is ∼3 km/s. The stress drop of the two asperities is 3 and 5 MPa, respectively, with a peak slip of ∼0.9 m. We find that the directivity controls the relatively amplitudes of displacement and velocity at stations ISKH01 and ISK001 (Figure S20 in Supporting Information S1). The comparison between synthetic waveforms and data suggests a preferred directivity of N50°E, close to the strike direction. This preferred model can fit the long-period waveform signatures, including total deformation durations and static displacements, but fails to explain the multiple wiggles at ISK001 (Figure S20 in Supporting Information S1).

The AMRFs in Figure 3 commonly suggest two energy pulses. However, the results are obtained with a lowpass filter of 1 Hz applied, which may wipe out high-frequency details. Moreover, AMRFs below 2 Hz generally feature more energy pulses. Therefore, we test dynamic rupture models with more asperities. As shown in Figure 4, the synthetics in the 6-asperity model much improve in fitting the displacement and velocity waveforms at stations ISK001 with multiple wiggles (Figures 4b and 4d). In our models, the amplitudes of wiggles depend on the energy release intensity at asperities with higher stress drops leading to larger velocity amplitudes (Figure S21 in Supporting Information S1). Based on the observed mild deformation onsets at both stations and following large velocity wiggles, we suggest that the rupture should involve a weak asperity initially and then break several strong asperities (Figure 4 and Figure S21 in Supporting Information S1). The energy radiated from those asperities overlaps in the forward side of rupture propagation (ISKH01) while being more separated as multiple peaks in the backward side (ISK001) (Figures 4b–4e). It is important to note that our objective is not to achieve perfect fitting on the waveforms or resolve detailed dynamic parameters. Rather, we aim to recover the first-order characteristics. Overall, the dynamic models, informed by near source strong-motion records, suggest a northeastward rupture with multiple asperities.

We further compare the source spectra of dynamic models with the observed source spectra of the M_W 5.7 event. Due to the presence of multiple energy pulses, the 6-asperity dynamic model shows a similar low average falloff rate in the frequency band of 0.5–2 Hz (Figure S22 in Supporting Information S1).

5. Discussion

The rupture of the M_W 5.7 event resides in the fluid-rich area. According to the catalog (Yoshida et al., 2024), the swarm had extended beneath the Noto peninsula before the occurrence of the 2023 M_W 5.7 event. The hypocenter and the possible rupture zone of the M_W 5.7 event are located inside the area of the persisting swarm (Figure S23 in Supporting Information S1). According to previous studies, the migration of the swarm seismicity has been commonly suggested to be associated with fluid diffusion in the fault system (e.g., Kato, 2024; Umeda et al., 2024; Yoshida et al., 2024). Therefore, we believe that the M_W 5.7 occurred under a fluid-rich condition. After the 2023 M5+ sequence, the swarm area remained active with a further up-dip seismicity migration (Figure S23 in Supporting Information S1).

The swarm and the multi-asperity rupture of the M_W 5.7 event suggest a heterogeneous stress condition in this fault system. Natural faults are inherently heterogeneous in fault geometry, material properties, and stress, which control fault slip behaviors. The involvement of fluids can further enhance the heterogeneity. Due to the intrinsic permeability variations, the distribution of fluids in the fault system is uneven, leading to spatially heterogeneous fault stress perturbation. Regions of elevated fluid pressure are weakened through a reduction of effective normal stress and frictional strength, which promotes aseismic or seismic fault slip (mostly as swarm events). Conversely, low-pore-pressure zones hold asperities that remain locked and accumulate stress. We interpret the M_W 5.7 as the rupture of several asperities that had been progressively loaded by the preceding swarm activity. The rupture started with a relatively weak asperity and occasionally triggered the breaking of a neighboring critically stressed strong asperity, leading to intense coseismic stress loading and cascading rupture of more asperities. This heterogeneous rupture process resulted in the prolonged high-frequency signals and the abnormal spectral decay rate in the frequency band of 0.5–2 Hz. Considering the spatial proximity to the 2024 M_W 7.5 event, we deduce that the long, weak radiation with enhanced high-frequency signals of the M_W 7.5 event may also be the manifestation of failures of small asperities under a similar local heterogeneous stress condition.

The small isolated multiple asperities have also been used to explain depth-dependent seismic radiation behaviors in subduction zones to reconcile the depth dependence of slip distribution and the high-frequency coherent radiators from teleseismic BP images for great megathrust events, such as in the 2011 Tohoku M_W 9.0 and the 2010 Chile M_W 8.8 events (Lay et al., 2012). The high-frequency content gets enhanced with depth according to spectral analyses for global large megathrust earthquakes (Ye et al., 2016) and for individual subduction zones (i.e., Ye et al., 2013). Such high-frequency enrichment has been proposed to be associated with consecutive breaking of isolated small-scale patches surrounded by the weak aseismic area (Lay et al., 2012; Ye et al., 2016). Similarly, the M_W 5.7 event broke multiple asperities in a fault zone weakened by fluids. Our observations and dynamic models demonstrate how multiple asperities can influence the high-frequency seismic signals and provide a quantitative modeling of this effect, although the number of asperities involved is limited.

Tectonic low-frequency earthquakes (LFEs) and very-low-frequency earthquakes (VLFs) also feature relatively low spectral decay rates with relatively weak but pronounced high-frequency seismic radiation (e.g., Ide et al., 2007; Plourde et al., 2015; Shelly et al., 2007). But due to the relatively long source durations and low corner frequencies, their high-frequency radiation is overall depleted compared to normal earthquakes with similar moment magnitudes. Ando et al. (2010) and Gomberg et al. (2016) also propose source models composed of a cluster of smaller events and/or tremors, in which the spectra slowly decay between the frequencies corresponding to the entire cluster duration and the characteristic duration of individual subevents. Our proposed multi-asperity model for the 2023 M_W 5.7 event is an analog to such VLF and LFE source models. The identified critical frequency of 2 Hz, above which the source spectrum of the M_W 5.7 event decays similarly to other M5+ events, corresponds to the rupture durations (∼0.5 s) of individual asperities (Figure 4).

6. Conclusion

In this study, we identify enhanced high-frequency seismic signals and an abnormally low spectral falloff rate for the 2023 M_W 5.7 event in the Noto swarm region. With the apparent moment-rate functions in the time domain and the dynamic modeling, constrained by the near-source strong-motion data, we propose that the enhanced high-frequency seismic radiation is due to the rupture of multiple isolated asperities in the relatively weak fluid-bearing fault zone. Such multi-asperity rupture model can explain the weak, prolonged seismic radiation with enhanced high-frequency content in the swarm region during the 15-s-long initial rupture of the 2024 M_W 7.5 earthquake (Ma et al., 2024; Xu et al., 2024), the enrichment of high-frequency content and slow spectral decay for large downdip megathrust earthquakes (Ye et al., 2013, 2016), the enhanced downdip high-frequency radiation in great megathrust events (Lay et al., 2012), and the slow spectral decay rates of LFEs and VLFs (Ando et al., 2010; Gomberg et al., 2016).

Conflict of Interest

The authors declare no conflicts of interest relevant to this study.

Data Availability Statement

The waveform data used in this study are strong-motion data recorded by networks of KiK-net and K-NET, which can be publicly accessed at https://www.kyoshin.bosai.go.jp/kyoshin/quake/index_en.html. The focal mechanisms used in this study are from the NIED catalog, which can be accessed at https://www.fnet.bosai.go.jp/event/search.php?LANG=en.

Acknowledgments

We thank Wenzheng Gong, Lingci Zeng, Shiqing Xu, and Thorne Lay for helpful discussions. We also thank the Editor Germán Prieto, the associate Editor Victor Tsai, the reviewer Qibin Shi, and one anonymous reviewer for their thoughtful comments and suggestions, which helped improve the manuscript. The work was supported in part by National Key R&D Program of China 2023YFF0803200, National Natural Science Foundation of China 42474077, and Hong Kong RGC Grants 14306122 and 14308523.

References

Aagaard, B. T., Knepley, M. G., & Williams, C. A. (2013). A domain decomposition approach to implementing fault slip in finite-element models of quasi-static and dynamic crustal deformation. *Journal of Geophysical Research: Solid Earth*, *118*(6), 3059–3079. https://doi.org/10.1002/jgrb.50217

Amezawa, Y., Hiramatsu, Y., Miyakawa, A., Imanishi, K., & Otsubo, M. (2023). Long-living earthquake swarm and intermittent seismicity in the northeastern tip of the Noto Peninsula, Japan. *Geophysical Research Letters*, *50*(8), e2022GL102670. https://doi.org/10.1029/2022gl102670

Ando, R., Nakata, R., & Hori, T. (2010). A slip pulse model with fault heterogeneity for low-frequency earthquakes and tremor along plate interfaces. *Geophysical Research Letters*, *37*(10), L10310. https://doi.org/10.1029/2010gl043056

Aochi, H. (2024). Dynamic rupture inversion on the *M*5.9 pre-event before the 2024 *M*7. 6 Noto-Peninsula, Japan, earthquake. *Earth Planets and Space*, *76*(1), 148. https://doi.org/10.1186/s40623-024-02095-4

Asano, K., & Iwata, T. (2025). Source rupture process of the M_W 6.2 earthquake in the Noto Peninsula, central Japan, on May 5, 2023. *Earth Planets and Space*, *77*(1), 1–15. https://doi.org/10.1186/s40623-025-02186-w

Brune, J. N. (1970). Tectonic stress and the spectra of seismic shear waves from earthquakes. *Journal of Geophysical Research*, *75*(26), 4997–5009. https://doi.org/10.1029/jb075i026p04997

Fujii, Y., & Satake, K. (2024). Slip distribution of the 2024 Noto Peninsula earthquake (MJMA 7.6) estimated from tsunami waveforms and GNSS data. *Earth Planets and Space*, *76*(1), 1–12. https://doi.org/10.1186/s40623-024-01991-z

Fukuoka, M., Hiramatsu, Y., & Yamada, T. (2024). Linking the spatiotemporal distribution of static stress drops to source faults in a fluid-driven earthquake swarm, northeastern Noto Peninsula, central Japan. *Earth Planets and Space*, *76*(1), 125. https://doi.org/10.1186/s40623-024-02074-9

Fukushima, Y., Ishimura, D., Takahashi, N., Iwasa, Y., Malatesta, L. C., Takahashi, T., et al. (2024). Landscape changes caused by the 2024 Noto Peninsula earthquake in Japan. *Science Advances*, *10*(49), eadp9193. https://doi.org/10.1126/sciadv.adp9193

Gomberg, J., Agnew, D. C., & Schwartz, S. Y. (2016). Alternative source models of very low frequency events. *Journal of Geophysical Research: Solid Earth*, *121*(9), 6722–6740. https://doi.org/10.1002/2016jb013001

Gong, W., Ye, L., Qiu, Y., Lay, T., & Kanamori, H. (2022). Rupture directivity of the 2021 M_W 6.0 Yangbi, Yunnan earthquake. *Journal of Geophysical Research: Solid Earth*, *127*(9), e2022JB024321. https://doi.org/10.1029/2022jb024321

Guo, Y., Miyakoshi, K., & Sato, T. (2024). Kinematic source rupture on listric faults for the 2024 Noto Peninsula, Japan, earthquake (M_W 7.5) estimated from near-field strong-motion waveforms. *Earth Planets and Space*, *76*(1), 177. https://doi.org/10.1186/s40623-024-02125-1

Hirose, F., Tamaribuchi, K., Kobayashi, A., & Maeda, K. (2024). Relation between earthquake swarm activity and tides in the Noto region, Japan. *Earth Planets and Space*, *76*(1), 37. https://doi.org/10.1186/s40623-024-01985-x

Ide, S., Beroza, G. C., Shelly, D. R., & Uchide, T. (2007). A scaling law for slow earthquakes. *Nature*, *447*(7140), 76–79. https://doi.org/10.1038/nature05780

Kato, A. (2024). Implications of fault-valve behavior from immediate aftershocks following the 2023 Mj6.5 earthquake beneath the Noto Peninsula, central Japan. *Geophysical Research Letters*, *51*(1), e2023GL106444. https://doi.org/10.1029/2023gl106444

Kumazawa, T., & Ogata, Y. (2024). Spatial and temporal variations of the 3-year earthquake swarm activities leading up to the *M*7.6 Noto Peninsula earthquake and interpretations of their activities. *Earth Planets and Space*, *76*(1), 164. https://doi.org/10.1186/s40623-024-02112-6

Kutschera, F., Jia, Z., Oryan, B., Wong, J. W. C., Fan, W., & Gabriel, A. A. (2024). The multi-segment complexity of the 2024 M_W 7.5 Noto Peninsula earthquake governs tsunami generation. *Geophysical Research Letters*, *51*(21), e2024GL109790. https://doi.org/10.1029/2024gl109790

Laske, G., Masters, G., Ma, Z., & Pasyanos, M. (2013). Update on CRUST1.0 – A 1-degree global model of Earth's crust. *Geophysical Research Abstracts*, *15*.

Lay, T., Kanamori, H., Ammon, C. J., Koper, K. D., Hutko, A. R., Ye, L., et al. (2012). Depth-varying rupture properties of subduction zone megathrust faults. *Journal of Geophysical Research*, *117*(B4), B04311. https://doi.org/10.1029/2011jb009133

Liu, C., Bai, Y., Lay, T., He, P., Wen, Y., Wei, X., et al. (2024). Shallow crustal rupture in a major M_W 7.5 earthquake above a deep crustal seismic swarm along the Noto Peninsula in western Japan. *Earth and Planetary Science Letters*, *648*, 119107. https://doi.org/10.1016/j.epsl.2024.119107

Ma, Z., Zeng, H., Luo, H., Liu, Z., Jiang, Y., Aoki, Y., et al. (2024). Slow rupture in a fluid-rich fault zone initiated the 2024 M_W 7.5 Noto earthquake. *Science*, *385*(6711), 866–871. https://doi.org/10.1126/science.ado5143

Matsumoto, R., & Yoshida, K. (2024). Quasi-real-time earthquake relocation and monitoring in the northeastern Noto Peninsula. *Earth Planets and Space*, *76*(1), 131. https://doi.org/10.1186/s40623-024-02079-4

Nakajima, J. (2022). Crustal structure beneath earthquake swarm in the Noto Peninsula, Japan. *Earth Planets and Space*, *74*(1), 160. https://doi.org/10.1186/s40623-022-01719-x

Nishimura, T., Hiramatsu, Y., & Ohta, Y. (2023). Episodic transient deformation revealed by the analysis of multiple GNSS networks in the Noto Peninsula, central Japan. *Scientific Reports*, *13*(1), 8381. https://doi.org/10.1038/s41598-023-35459-z

Ogata, Y., & Kumazawa, T. (2024). Inverse analysis of seismic activity rate changes for severely incomplete sequences: Comparison of aftershock activity patterns immediately following the 2023 *M*6. 5 and 2024 *M*7. 6 Noto Peninsula earthquakes. *Earth Planets and Space*, *76*(1), 112. https://doi.org/10.1186/s40623-024-02057-w

Okada, T., Savage, M. K., Sakai, S. I., Yoshida, K., Uchida, N., Takagi, R., et al. (2024). Shear wave splitting and seismic velocity structure in the focal area of the earthquake swarm and their relation with earthquake swarm activity in the Noto Peninsula, central Japan. *Earth Planets and Space*, *76*(1), 24. https://doi.org/10.1186/s40623-024-01974-0

Okuwaki, R., Yagi, Y., Murakami, A., & Fukahata, Y. (2024). A multiplex rupture sequence under complex fault network due to preceding earthquake swarms during the 2024 M_W 7.5 Noto Peninsula, Japan, earthquake. *Geophysical Research Letters*, *51*(11), e2024GL109224. https://doi.org/10.1029/2024gl109224

Peng, Z., Lei, X., Wang, Q. Y., Wang, D., Mach, P., Yao, D., et al. (2025). The evolution process between the earthquake swarm beneath the Noto Peninsula, central Japan and the 2024 *M*7.6 Noto Hanto earthquake sequence. *Earthquake Research Advances*, *5*(1), 100332. https://doi.org/10.1016/j.eqrea.2024.100332

Plourde, A. P., Bostock, M. G., Audet, P., & Thomas, A. M. (2015). Low-frequency earthquakes at the southern Cascadia margin. *Geophysical Research Letters*, *42*(12), 4849–4855. https://doi.org/10.1002/2015gl064363

Shelly, D. R., Beroza, G. C., & Ide, S. (2007). Non-volcanic tremor and low-frequency earthquake swarms. *Nature*, *446*(7133), 305–307. https://doi.org/10.1038/nature05666

Shinohara, M., Hino, R., Takahashi, T., Obana, K., Kodaira, S., Azuma, R., et al. (2025). Precise aftershock activity in the marine source region of the 2024 Noto-Hanto earthquake by rapid response observation using ocean bottom seismometers. *Earth Planets and Space*, *77*(1), 43. https://doi.org/10.1186/s40623-025-02171-3

Suppasri, A., Kitamura, M., Alexander, D., Seto, S., & Imamura, F. (2024). The 2024 Noto Peninsula earthquake: Preliminary observations and lessons to be learned. *International Journal of Disaster Risk Reduction*, *110*, 104611. https://doi.org/10.1016/j.ijdrr.2024.104611

Takano, S., Hiramatsu, Y., & Yukutake, Y. (2024). The role of fluids in earthquake swarms in northeastern Noto Peninsula, central Japan: Insights from source mechanisms. *Earth Planets and Space*, *76*(1), 151. https://doi.org/10.1186/s40623-024-02099-0

Umeda, K., Yamazaki, Y., & Sumino, H. (2024). Geochemical signature of deep fluids triggering earthquake swarm in the Noto Peninsula, central Japan. *Geophysical Research Letters*, *51*(13), e2024GL108581. https://doi.org/10.1029/2024gl108581

Wang, Q. Y., Cui, X., Frank, W. B., Lu, Y., Hirose, T., & Obara, K. (2024). Untangling the environmental and tectonic drivers of the Noto earthquake swarm in Japan. *Science Advances*, *10*(19), eado1469. https://doi.org/10.1126/sciadv.ado1469

Xu, L., Ji, C., Meng, L., Ampuero, J. P., Yunjun, Z., Mohanna, S., & Aoki, Y. (2024). Dual-initiation ruptures in the 2024 Noto earthquake encircling a fault asperity at a swarm edge. *Science*, *385*(6711), 871–876. https://doi.org/10.1126/science.adp0493

Yamada, T., Ohta, Y., Nishimura, T., Yoshida, K., Hiramatsu, Y., & Kinoshita, Y. (2025). Coseismic slip distribution of the 2024 Noto Peninsula earthquake deduced from dense global navigation satellite system network and interferometric synthetic aperture radar data: Effect of assumed dip angle. *Earth Planets and Space*, *77*(1), 19. https://doi.org/10.1186/s40623-025-02154-4

Yamanaka, Y., Matsuba, Y., Shimozono, T., & Tajima, Y. (2024). Nearshore propagation and amplification of the tsunami following the 2024 Noto Peninsula earthquake, Japan. *Geophysical Research Letters*, *51*(19), e2024GL110231. https://doi.org/10.1029/2024gl110231

Yang, S., Sang, C., Hu, Y., & Wang, K. (2024). Coseismic and early postseismic deformation of the 2024 M_W 7.45 Noto Peninsula earthquake. *Geophysical Research Letters*, *51*(11), e2024GL108843. https://doi.org/10.1029/2024gl108843

Ye, L., Kanamori, H., Rivera, L., Lay, T., Zhou, Y., Sianipar, D., & Satake, K. (2020). The 22 December 2018 tsunami from flank collapse of Anak Krakatau volcano during eruption. *Science Advances*, *6*(3), eaaz1377. https://doi.org/10.1126/sciadv.aaz1377

Ye, L., Lay, T., & Kanamori, H. (2013). Ground shaking and seismic source spectra for large earthquakes around the megathrust fault offshore of northeastern Honshu, Japan. *Bulletin of the Seismological Society of America*, *103*(2B), 1221–1241. https://doi.org/10.1785/0120120115

Ye, L., Lay, T., Kanamori, H., & Rivera, L. (2016). Rupture characteristics of major and great ($M_W \geq 7.0$) megathrust earthquakes from 1990 to 2015: 2. Depth dependence. *Journal of Geophysical Research: Solid Earth*, *121*(2), 845–863. https://doi.org/10.1002/2015jb012427

Yoshida, K., Takagi, R., Fukushima, Y., Ando, R., Ohta, Y., & Hiramatsu, Y. (2024). Role of a hidden fault in the early process of the 2024 M_W 7.5 Noto Peninsula earthquake. *Geophysical Research Letters*, *51*(16), e2024GL110993. https://doi.org/10.1029/2024gl110993

Yoshida, K., Uchida, N., Matsumoto, Y., Orimo, M., Okada, T., Hirahara, S., et al. (2023). Updip fluid flow in the crust of the northeastern Noto Peninsula, Japan, triggered the 2023 M_W 6.2 Suzu earthquake during swarm activity. *Geophysical Research Letters*, *50*(21), e2023GL106023. https://doi.org/10.1029/2023gl106023

Yoshida, K., Uno, M., Matsuzawa, T., Yukutake, Y., Mukuhira, Y., Sato, H., & Yoshida, T. (2023). Upward earthquake swarm migration in the northeastern Noto Peninsula, Japan, initiated from a deep ring-shaped cluster: Possibility of fluid leakage from a hidden magma system. *Journal of Geophysical Research: Solid Earth*, *128*(6), e2022JB026047. https://doi.org/10.1029/2022jb026047